



## Review

# Experimental study and finite element analysis of a buckling-restrained brace consisting of three steel tubes with slotted holes in the middle tube



Zhang Dongbin<sup>a</sup>, Nie Xin<sup>a</sup>, Pan Peng<sup>b,\*</sup>, Wang Mengzi<sup>a</sup>, Deng Kailai<sup>a</sup>, Chen Yabin<sup>a</sup>

<sup>a</sup> Civil Engineering Department, Tsinghua University, Beijing 100084, China

<sup>b</sup> Key Laboratory of Civil Engineering Safety and Durability of China Education Ministry, Tsinghua University, Beijing 100084, China

## ARTICLE INFO

## Article history:

Received 15 January 2016

Received in revised form 5 May 2016

Accepted 6 May 2016

Available online 21 May 2016

## Keywords:

Buckling-restrained brace

Three steel tubes

Slotted hole

Cyclic loading test

Finite element analysis

## ABSTRACT

A novel buckling-restrained brace comprising three circular steel tubes with different diameters is proposed. The three tubes overlap, and the inner and outer tubes restrain the out-of-plane deformation of the middle tube. Slotted holes are arranged on the middle tube. This BRB has a much larger energy dissipation area and can be conveniently fabricated. The size and number of slotted holes on the middle tube were adopted as test parameters. Five different specimens were tested by using quasi-static cyclic loading schemes to investigate the strength, deformation capacity, hysteretic behavior and failure mode of the new buckling-restrained brace. Nonlinear finite element analyses using ABAQUS were carried out in detail to explain the load-deflection hysteresis curves and modes of failure obtained in all five experiments. According to the tests and finite element analyses results, the structure of the novel buckling-restrained brace is reasonable and effective. When the opening-hole ratio is 0.2 and  $2 \times 2$  slotted holes are arranged on the middle tube, the buckling-restrained brace exhibits excellent performance in terms of its deformation capacity and low-cycle fatigue behavior. The hysteresis curves of the braces are stable and saturated, and correspond to an equivalent ratio of critical viscous damping of 0.40 at the loading amplitude of 1/100L.

© 2016 Elsevier Ltd. All rights reserved.

## Contents

1. Introduction . . . . .	1
2. Experimental study . . . . .	2
2.1. Details of the triple-steel-tube BRB. . . . .	2
2.2. Test scheme . . . . .	2
2.3. Deformation and failure modes . . . . .	3
2.4. Hysteretic performance. . . . .	5
2.5. Equivalent ratio of critical viscous damping. . . . .	6
3. Finite element (FE) analyses . . . . .	6
3.1. Verification of the FE model. . . . .	6
3.2. Effect of the opening-hole ratio $v$ . . . . .	7
3.3. Effect of the opening-hole number. . . . .	7
4. Conclusion . . . . .	9
Acknowledgements . . . . .	9
References . . . . .	10

## 1. Introduction

The application of braces in a high-rise building is an effective way of resisting seismic forces. Marino E M and Nakashima M [1] researched on

the seismic design of steel-braced frames in which the braces are configured in a chevron pattern, which could control the maximum inter-story drift. The traditional brace provides good performance in the event of a small earthquake, but it is prone to global and local buckling and even low-cycle fatigue fracture in the event of a large earthquake. Such damage to the brace severely reduces the ability of the brace to dissipate energy. In recent years, the buckling-restrained brace (BRB) has

\* Corresponding author.

E-mail address: panpeng@mail.tsinghua.edu.cn (P. Peng).

been widely used as a new type of brace in high-rise buildings. Bosco M and Marino E M [2] proposed a design procedure and behavior factor for steel frames with buckling-restrained braces. The BRB provides high stiffness and strength like the traditional brace and has large energy dissipation capacity like a steel damper. During earthquakes, the BRB can achieve material yield of the entire cross-section rather than global buckling under compression, thus it is effective in terms of dissipating earthquake energy and protecting the main structure. As an effective energy dissipation device, the BRB has been suggested as a solution for improving the seismic performance of buildings and has been widely used in China after the Wenchuan earthquake [3].

In recent decades, there have been breakthroughs in research on the BRB. In the 1970s, Kimura [4] first proposed the concept of the BRB and performed experiments that showed that the BRB has good energy dissipation. In the 1990s, Kuwahara [5] proposed a new structure in which an outer steel tube bore the axial force and a kernel steel tube acted as a constraint unit. Suzuki [6] analyzed the clearance of inner and outer steel tubes and the diameter–thickness ratio for a double-steel-tube BRB. Takeita K et al. [7] proposed a triple-tube BRB and showed that it was a good energy dissipation damping component. Hasegawa et al. [8] performed a shaking-table test and low-cycle fatigue test for the BRB, verifying its high dissipation capacity. Koetaka et al. [9] proposed a criterion of BRBs for the prevention of out-of-plane buckling and revealed that the connector stiffness affects global buckling. Xie et al. [10] presented important issues of BRB configurations, such as the gap and debonding process between core braces and encasing members. Hoveidae et al. [11] conducted a parametric study of BRBs with different gaps and initial imperfections and found that buckling restraining mechanisms affect the global buckling behavior. Ye et al. [12] summarized design methods and conducted a series of performance tests. Guo et al. [13,14] investigated the global mechanical properties of BRBs for different boundary conditions, showing that the fixed boundary condition provided better performance than the pinned boundary condition. Yin et al. [15] improved the kernel structure of the double-steel-tube BRB and showed that the design of a double-steel-tube BRB with a contact ring prevented the kernel and outer tubes from buckling. Deng and Zhou [16,17] designed new triple-steel-tube BRBs with local holes and slots, and conducted tests and finite element analysis to demonstrate the good performance and stable energy dissipation capacity of their designs.

Following on the above studies of the triple-steel-tube BRB, the present paper proposes a new BRB consisting of three steel tubes

with slotted holes in the middle tube. This BRB has a much larger energy dissipation area and can be conveniently fabricated. Full scale tests are conducted for five different specimens to investigate the effect of the different sizes and numbers of slotted holes on the strength, deformation capacity, hysteresis behavior, backbone curve, and failure mode of the BRB. Nonlinear finite element analyses using ABAQUS were carried out in detail to explain the load-deflection hysteresis curves and modes of failure obtained in all five experiments.

## 2. Experimental study

### 2.1. Details of the triple-steel-tube BRB

As shown in Fig. 1, the triple-steel-tube consists of three circular steel tubes; i.e., an inner tube, middle tube and outer tube. The three circular tubes have different diameters, and there is no unbonded material between them. The dimensions of the inner, middle and outer tubes are 2900 mm × 140 mm × 6 mm, 3000 mm × 159 mm × 8 mm and 1430 mm × 180 mm × 9 mm, respectively. The gap between the inner and middle tubes and that between the middle and outer tubes are both 1.5 mm. The length of the slotted hole is 1300 mm. The middle tube is the main component that bears the axial force. The section of slotted holes is expected to yield, and thus reduce the stress and deformation at the end of the BRB. The inner and outer tubes are used as constraint units to prevent compressive buckling of the middle tube, so that it provides the best energy dissipation capacity. The outer tube is divided into two parts, and the inner tube is kept as one part. The inner tube and outer tube are connected with the middle tube at the mid-span by spot welding, mainly to maintain the relative positions of the three tubes. All the steel tubes were made of Q235 steel. A coupon test revealed that the steel has a yield strength  $f_y$  of 422 MPa, ultimate strength  $f_u$  of 639 MPa, and elongation ratio of 20%.

### 2.2. Test scheme

Quasi-static tests were conducted to verify the performance of the novel BRB. In total, five specimens, named B1 to B5, were tested. Each specimen had the same-sized steel tubes. In the tests, the number of slotted holes  $n$  and the opening-hole ratio  $v$  were major parameters.

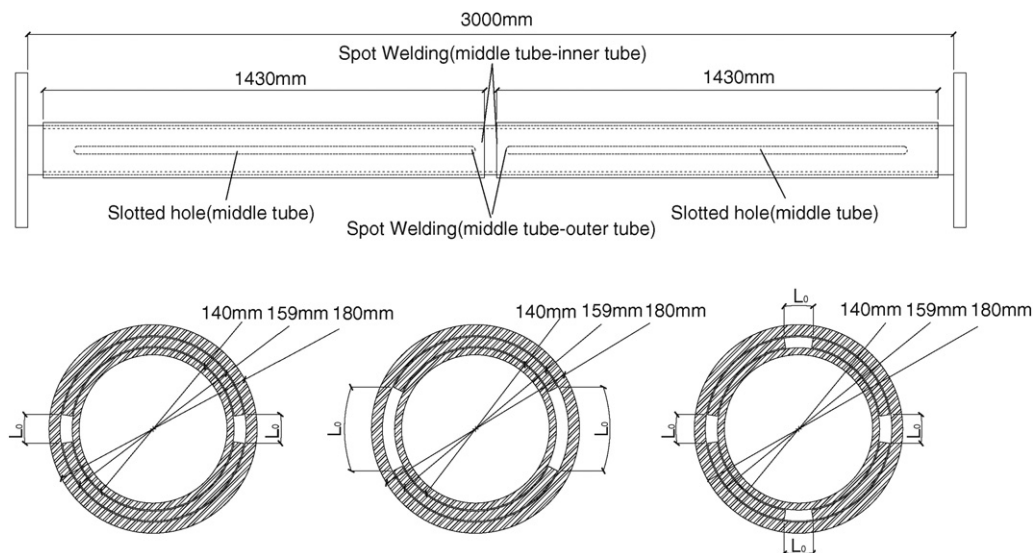


Fig. 1. Structure of the BRB.

**Table 1**  
Parameters of the five specimens.

No.	$n$	$v$	Remark
B1	$2 \times 2$	0.1	Compared specimen ( $v$ )
B2	$2 \times 2$	0.2	Standard specimen
B3	$2 \times 2$	0.3	Compared specimen ( $v$ )
B4	$2 \times 2$	0.5	Compared specimen ( $v$ )
B5	$2 \times 4$	0.2	Compared specimen ( $n$ )

The opening-hole ratio is defined as

$$v = \frac{nL_0}{C} \quad (1)$$

where  $L_0$  is the arc length of one slotted hole and  $C$  is the perimeter of the middle tube (refer to Fig. 1). As shown in Table 1, B2 is the standard specimen. B1, B2, B3 and B4 have the same number of slotted holes but different opening-hole ratios. B2 and B5 have the same opening-hole ratio but different numbers of slotted holes.

The loading setup, consisting of an actuator, a foundation beam and two shear keys, is shown in Fig. 2. The foundation beam was tied down to the strong floor with anchor bolts, and the two shear keys were connected to the foundation beam using high-strength bolts. The specimen was connected to the actuator and the shear key using high-strength bolts.

The loading uses displacement control and the loading scheme is shown in Fig. 3. The loading amplitude was increased to  $1/300L$ ,  $1/200L$ ,  $1/150L$ ,  $1/100L$  and  $1/75L$ . Here,  $L$  is the length of the BRB; i.e., 3000 mm in this case. For the loading amplitudes of  $1/300L$ ,  $1/200L$  and  $1/150L$ , the specimens were loaded in three cycles. For the loading amplitude of  $1/100L$ , the specimens were loaded in 30 cycles. Finally, specimens were loaded at the loading amplitude of  $1/75L$  until the bearing capacity of the brace decreased to 85% of the corresponding peak bearing capacity.

As shown in Fig. 2, nine displacement transducers, designated D1 to D9, were installed to measure the displacements of the specimens. D1 and D2 recorded the axial deformation of the specimen, while D3–D9 were installed along the specimens to record the out-of-plane deformation of the specimens.

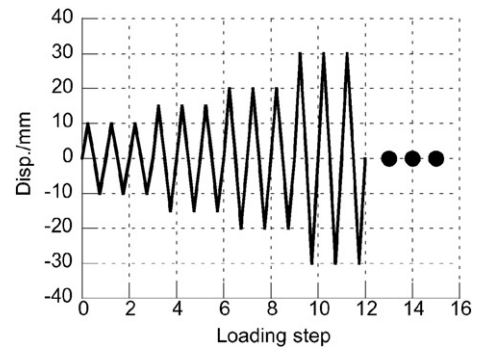


Fig. 3. Loading scheme.

### 2.3. Deformation and failure modes

The deformation and failure modes of B1 to B5 are shown in Fig. 4(a)–(e), respectively. Three failure modes are observed; i.e., local buckling at the end, tension failure at the slotted hole, and global buckling.

B2 is the standard specimen. Global buckling occurred in compression under the loading amplitude of  $1/75L$  (40 mm), as shown in Fig. 4(b). With the increase in loading amplitude, the plastic deformation of the slotted-hole field became more concentrated and the friction between the middle tube and the constraint tubes increased. Finally the axial force exceeded the buckling load and led to the global buckling failure of the specimen.

B1 has a smaller opening-hole ratio than B2. Local buckling and tension failure occurred at the unconstrained end under compression at the loading amplitude of  $1/75L$ , as shown in Fig. 4(a). Owing to the small opening-hole ratio of B1, the fields with slotted holes have a yield strength similar to that of the fields with no holes. After a few cycles of loading, the fields with slotted holes yielded and showed strength hardening, leading to the axial force of the fields with slotted holes exceeding the local buckling load of the unconstrained end. Therefore, local buckling and tension failure occurred at the unconstrained end for B1.

B3 and B4 have a larger opening-hole ratio than B2. Tension fracture occurred at the end of the slotted holes under the loading amplitude of  $1/100L$ , as shown in Fig. 4(c) and (d), respectively. It is obvious that the field of slotted holes bears most of the deformation.

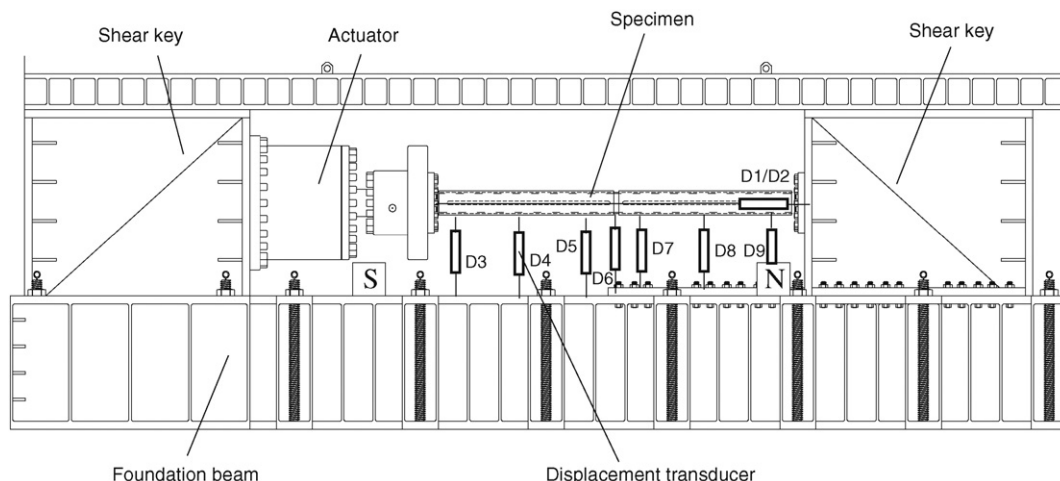


Fig. 2. Details of the test setup.

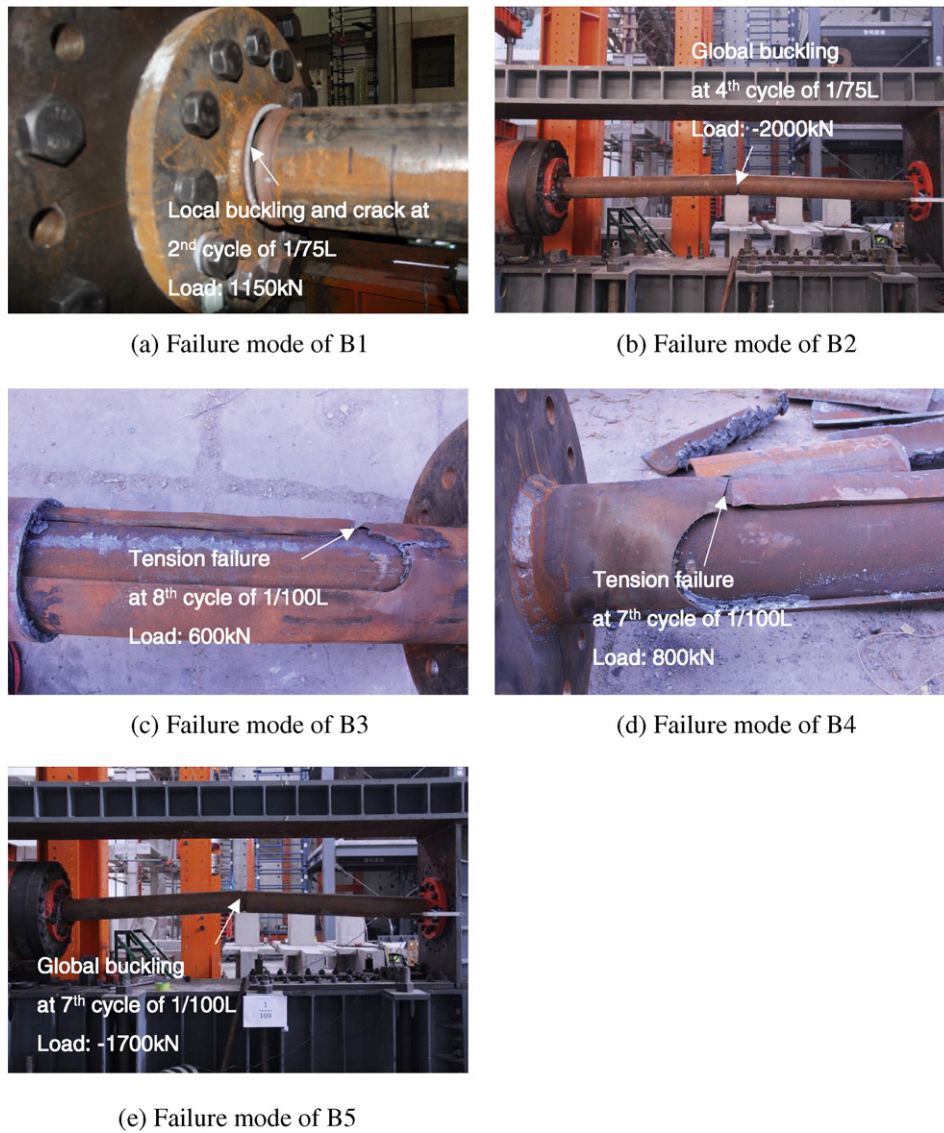


Fig. 4. Failure modes of specimens.

However, because of the large opening-hole ratio, there was a significant stress concentration at the end of the slotted holes, leading to an early fracture.

B5 has the same opening-hole ratio as B2, but it has more holes than B2. Global buckling occurred in the seventh cycle under the loading amplitude of  $1/100L$ . Because of the increase in the opening-hole number, the bending stiffness of the inner tube decreased, which reduced the constraint effect. Therefore, global buckling happened much earlier for B5 than for B2, as shown in Fig. 4(e).

Table 2 summarizes the failure modes, yield displacement and low-cycle number under  $1/100L$  and  $1/75L$  loading amplitudes. The yield displacements ranged 5.0–6.0 mm. With an increase in the opening-hole ratio, the yield displacement decreased owing to the decrease in the relative axial stiffness of the slotted-hole field to no-hole field. When the opening-hole ratio was low (e.g. the ratio for B1), the fatigue performance was basically satisfactory. However, there was local buckling at the unconstrained end because of strength hardening of the field with slotted holes. When the opening-hole ratio was appropriate (e.g., the ratio for B2), the fatigue performance was better, and finally, the increase in friction between

the middle tube and the constraint tubes resulted in global buckling. When the opening-hole ratio was too large (e.g., the ratios for B3 and B4), there was a fracture at the end of the slotted holes because of the deformation concentration. For the same opening-hole ratio, increasing the opening-hole number lowered the bending stiffness, which resulted in earlier global buckling.

Table 2  
Failure modes and low-cycle fatigue performance.

No.	Failure mode	Yield disp. mm	Low-cycle number	
			1/100L	1/75L
B1	Local buckling at the end with no constraint	6	30	2
B2	Global buckling	5.5	30	4
B3	Tension failure at the slotted hole	5	8	–
B4	Tension failure at the slotted hole	5	7	–
B5	Global buckling	5.5	7	–

2.4. Hysteretic performance

The hysteresis curves of the five specimens are summarized in Fig. 5(a)–(e). In the figures, the horizontal axis is the average displacement measured by the displacement transducers D1 and D2, while the vertical axis is the reaction force exerted by the actuator, where tension is positive and compression is negative.

As shown in Fig. 5(a), the hysteresis curve of B1 is stable and saturated. B1 underwent 30 cycles of loading at the loading amplitude of 1/100L and two cycles of loading at the loading amplitude of 1/75L. The reaction force decreased in the second cycle of loading at the

loading amplitude of 1/75L because the unconstrained end of the BRB cracked as a result of local buckling.

Fig. 5(b) shows the hysteresis curve of B2, which is also stable and saturated. B2 underwent 30 cycles of loading at a loading amplitude of 1/100L (30 mm) and four cycles of loading at a loading amplitude of 1/75L (40 mm). However, in the end, the reaction force of B2 decreased sharply because of global buckling under compression.

The hysteresis curves of B3 and B4 are shown in Fig. 5(c) and (d), respectively, and are stable and saturated when the loading amplitude is less than 1/100L. The reaction forces of B3 and B4 decreased

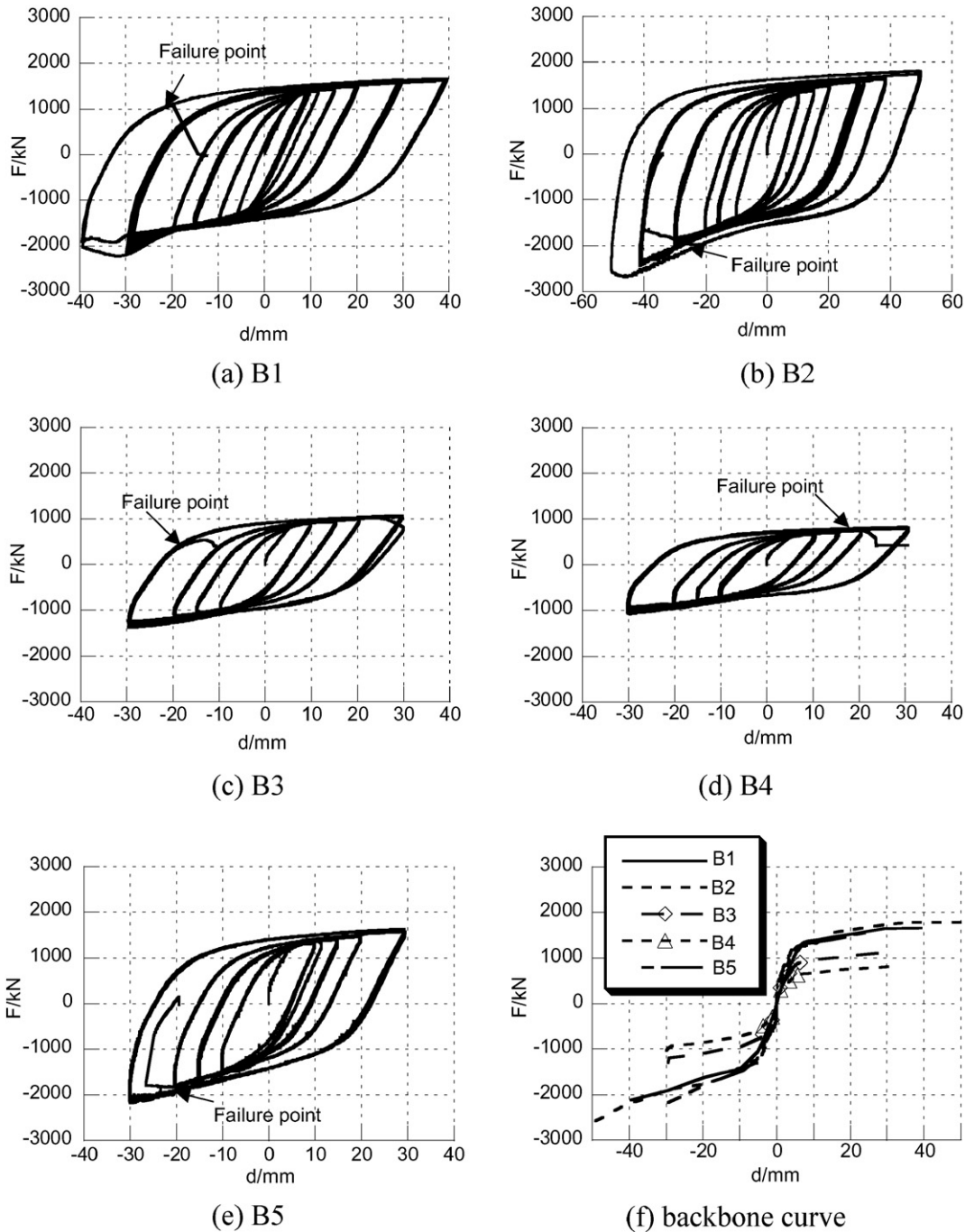


Fig. 5. Hysteresis curve and backbone curve.

**Table 3**  
Property parameters of the specimens.

No.	$P_{\max}$ at 1/100L		$\beta$	$\omega$	$K_1$ kN/mm	$K_2$ kN/mm	$K_3$ kN/mm
	$P_{t\max}$ /kN	$P_{c\max}$ /kN					
B1	1608	1752	1.09	1.28	258.91	14.67	28.28
B2	1469	1720	1.17	1.32	237.48	13.01	31.61
B3	1069	1290	1.21	1.26	165.74	11.76	20.27
B4	808	985	1.22	1.25	118.66	8.52	18.70
B5	1462	1697	1.16	1.31	239.8	14.30	36.47

in the eighth and seventh cycles of loading under the loading amplitude of 1/100L respectively, as a result of deformation concentration at the end of the slotted holes.

Fig. 5(e) shows the hysteresis curve of B5. The bearing capacity is lost in the seventh cycle of loading under the loading amplitude of 1/100L, which is because of global buckling.

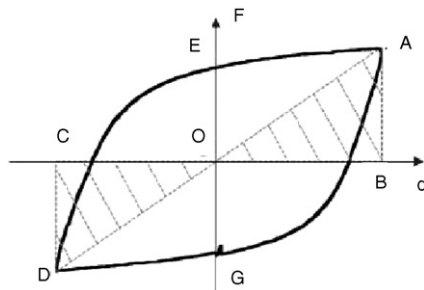
As shown in Fig. 5(f), backbone curves are obtained from the hysteresis curves of B1 to B5. In the initial time of the 1/100L loading amplitude, backbone curves of all the specimens are symmetrical in tension and compression. With the loading amplitude increasing, the reaction force in compression is obviously larger than that in tension. This is because, with the increase in compressive deformation, the middle tube deformed and contacted to the constraint tubes, resulting in large friction. There was much less friction when the BRB sustained tension, and the reaction force in compression and tension thus became severely asymmetrical.

Table 3 gives the ultimate force in the first cycle of 1/100L loading amplitude, tension–compression asymmetry coefficient  $\beta$ , tension strain hardening coefficient  $\omega$ , elastic stiffness  $K_1$  and hardening stiffness in tension and compression  $K_2$  and  $K_3$ . The tension–compression asymmetry coefficient  $\beta$  and tension strain hardening coefficient  $\omega$  are defined as

$$\beta = \frac{P_{c\max}}{P_{t\max}}, \quad (2)$$

$$\omega = \frac{P_{t\max}}{f_y A_0}, \quad (3)$$

where  $P_{c\max}$  and  $P_{t\max}$  are respectively the ultimate forces in compression and tension,  $A_0$  is the section area of the slotted holes,  $d_u$  and  $d_y$  are the ultimate and yield displacements, respectively,  $\beta$  reflects the degree of tensile and compressive bearing capacity asymmetry and  $\omega$  reflects the degree of strain hardening [18]. For the purpose of comparison, the data in the first cycle of the 1/100L loading amplitude was chosen to calculate  $\beta$  and  $\omega$ .



**Fig. 6.** Calculation of equivalent ratio of critical viscous damping.

**Table 4**  
Equivalent ratios of critical viscous damping.

Disp.	Equivalent ratios of critical viscous damping				
	B1	B2	B3	B4	B5
L/300 (10 mm)	0.24	0.30	0.24	0.27	0.29
L/200 (15 mm)	0.29	0.35	0.32	0.34	0.32
L/150 (20 mm)	0.34	0.36	0.35	0.37	0.35
L/100 (30 mm)	0.36	0.40	0.39	0.40	0.38
L/75 (40 mm)	0.41	0.42	–	–	–

For the 1/100L loading amplitude,  $\beta$  was in the range of 1.09–1.22, showing tension and compression asymmetry.  $\beta$  increased with the increase in the opening-hole ratio owing to larger deformation at the slotted holes, which led to greater friction in compression. For the 1/100L loading amplitude,  $\omega$  was in the range of 1.25–1.32, revealing that greater strain hardening occurred at the slotted holes. The elastic stiffness was in the range of 118–258 kN/mm, and yield stiffness in compression and tension was about 5.0%–16.0% of the elastic stiffness, respectively.

### 2.5. Equivalent ratio of critical viscous damping

According to the Chinese seismic design code of buildings GB5001-2010 [19], the equivalent ratio of critical viscous damping of the BRB is defined as Eq. (4), where  $W_c$  is the energy dissipated in a cycle for a given displacement, and  $W_s$  is the elastic strain energy for a given displacement.

$$\xi_{\text{eq}} = \frac{W_c}{4\pi W_s} \quad (4)$$

Specifically, it can be calculated according to Fig. 6 and Eq. (5). In reference to the figure,  $S_{\text{AGDEA}}$  in the equation is the area surrounded by the hysteresis curve, i.e. the dissipation of energy, and  $S_{\Delta OAB} + S_{\Delta OCD}$  in the equation is the summation of the area of  $\Delta OAB$  and  $\Delta OCD$ , i.e. the elastic strain energy.

$$\xi_{\text{eq}} = \frac{S_{\text{AGDEA}}}{2\pi(S_{\Delta OAB} + S_{\Delta OCD})} \quad (5)$$

The equivalent ratio of critical viscous damping of specimens at different loading amplitudes was obtained, as presented in Table 4. It is found that the equivalent ratio of critical viscous damping increased gradually with the increase in the loading amplitude. At the same loading amplitude, the equivalent ratio of critical viscous damping increased with the increase in the opening-hole ratio because of larger deformation of the slotted holes. At the same opening-hole ratio, with the opening-hole number increasing, the equivalent ratio of critical viscous damping of B2 and B5 hardly changed. B1 could provide an equivalent ratio of critical viscous damping of more than 0.24 and B2 could provide an equivalent ratio of critical viscous damping of more than 0.30.

## 3. Finite element (FE) analyses

### 3.1. Verification of the FE model

To supplement the physical test results, finite element analyses were conducted. The general FE software ABAQUS was adopted for the simulation. As shown in Fig. 7, the tube was simulated with a four-node shell element with reduced integration, designated as S4R in ABAQUS. Considering the efficiency of calculation and the difficulty of simulating contact between the tubes, only the middle tube was modeled, and the out-

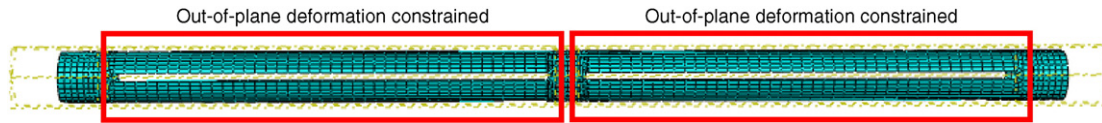


Fig. 7. Finite element model.

of-plane translational degrees of freedom were constrained for the parts having the slotted holes. The top and bottom ends of the middle tube were fixed.

As shown in a previous study, the mechanical behavior of steel under cyclic loading is different from that under monotonic loading [20]. Therefore, a constitutive model provided by ABAQUS for metal under cyclic loading was adopted; the effectiveness of the model has been demonstrated in previous studies [21,22]. The back stress formula of the material model provided by ABAQUS is

$$\alpha = \sum_{k=1}^n \frac{C_k}{\gamma_k} (1 - e^{-\gamma_k \bar{\epsilon}^{pl}}) \quad (6)$$

where  $\alpha$  represents the back stress, which indicates the movement of the yield surface,  $\bar{\epsilon}^{pl}$  is the equivalent plastic strain (PEEQ), and  $C_k$  and  $\gamma_k$  ( $k = 1, 2, 3$ ) are parameters of the model.  $\sum C_k/\gamma_k$  was the ultimate kinematic hardening stress [23]. In the FEM analysis, the initial yield stress was 422 MPa. Young's modulus and Poisson's ratio were 206 GPa and 0.3, respectively. The associated  $C_k$  and  $\gamma_k$  ( $k = 1, 2, 3$ ) are determined based on the stress-strain curve obtained from the coupon test, and the details about the parameters are given in Table 5. The stress-strain relationship obtained from the coupon test, and that obtained from the numerical calculation using the parameters given in Table 5 are plotted in Fig. 8. In the figure, the X-coordinate is the plastic strain and Y-coordinate is the hardening stress. It can be observed that the result obtained from the coupon test and that obtained from the numerical calculation agree well, demonstrating the effectiveness of the material model and correctness of the parameters.

Fig. 9 compares the physical test with the finite element analyses for B1–B5. Fig. 9(a), (c), (e), (g) and (i) compare the hysteresis curves of B1–B5, where the vertical axis is the axial force, with tension being positive and compression negative, and the horizontal axis is the axial deformation. Fig. 9(b), (d), (f), (h) and (j) show the PEEQ distributions of B1–B5. According to the hysteresis curves, the FE analysis results agree well with the results from the physical tests. Because the contact with the outer tube and inner tube was not modeled, the increase in the axial force in compression which resulted from the friction between the tubes cannot be observed. As shown in Fig. 9(b), the PEEQ at the unconstrained end is appreciably larger than that at other locations because of local buckling. In Fig. 9(f) and (h), the PEEQ at the end of the slotted hole is much larger than that at other locations because of stress concentration. These observations agree well with the physical test results of B1, B3 and B4. In Fig. 9(d) and (j), which correspond to the tests of B2 and B5, respectively, the global buckling could not be simulated because the out-of-plan deformation was constrained. It is observed that the FE models can generally simulate the

deformation and stress distribution of the middle tube if the tube is not damaged in global buckling.

### 3.2. Effect of the opening-hole ratio $v$

Local models of B1–B4 were established to analyze the effect of the opening-hole ratio  $v$ , where part of the middle tube was selected and designated as S4R in ABAQUS. The out-of-plane deformation of the slotted holes was constrained. The top and bottom of the part were fixed.

As shown in Fig. 10(a), the PEEQ distributions of B1–B4 were obtained under one cyclic loading at an amplitude of 10 mm. PEEQ distribution curves were obtained as shown in Fig. 10(b).

With an increase in the opening-hole ratio  $v$ , the deformation decreased in the unconstrained field and increased in the slotted-hole field. When the opening-hole ratio was 0.1, the deformation was concentrated in the unconstrained field, and there was local buckling as seen in the physical test of B1. When the opening-hole ratio increased, the deformation was concentrated to the slotted hole and increased, and the PEEQ at the end of the slotted hole was the largest, resulting in the damage seen in the physical tests of B3 and B4. Finally, according to the physical tests and FE analysis, an opening-hole ratio of 0.2 is recommended.

### 3.3. Effect of the opening-hole number

B2 and B5 have the same opening-hole ratio but different opening-hole numbers. In the physical tests, B5 underwent earlier global buckling failure. Obviously, the opening-hole number strongly affects the global stability of the BRB.

A previous study found that, for a BRB, the global buckling force should always be higher than the yield force of the kernel unit so as to protect the BRB from global buckling [24]. The constraint ratio  $\zeta$  was defined as

$$\zeta = \frac{P_{cr}}{F_y} = \left( \frac{\pi^2}{(\mu_i L_i)^2} E_i I_i + \sum \frac{\pi^2}{(\mu_0 L_0)^2} E_0 I_0 \right) / A_i f_y \quad (7)$$

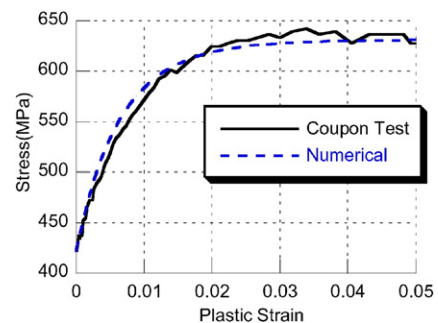


Fig. 8. Coupon test and numerical material model.

**Table 5**  
Material parameters used in ABAQUS model.

$C_1$	$\gamma_1$	$C_2$	$\gamma_2$	$C_3$	$\gamma_3$
$9 \times 10^9$	250	$2 \times 10^{10}$	150	$4 \times 10^9$	100

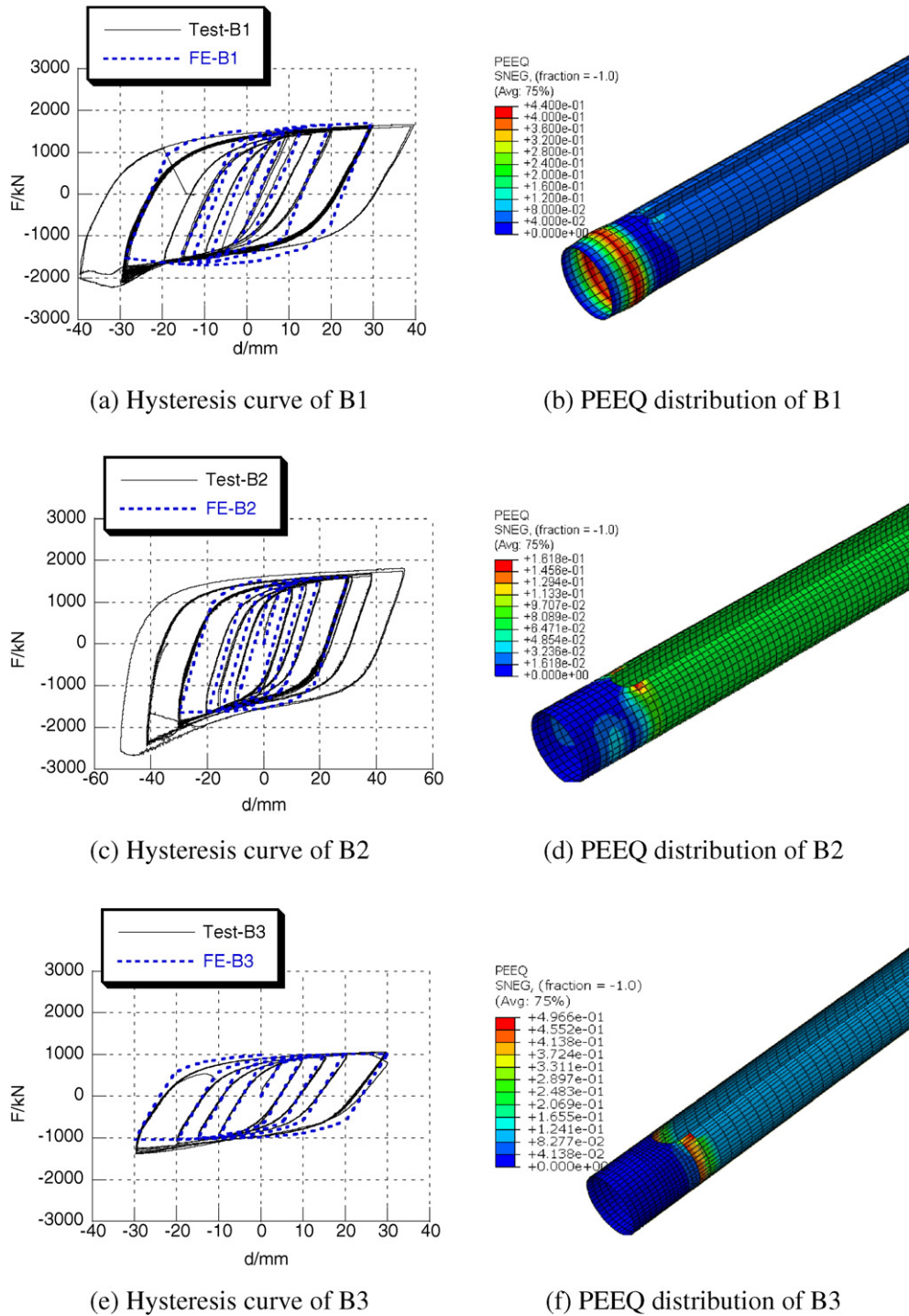


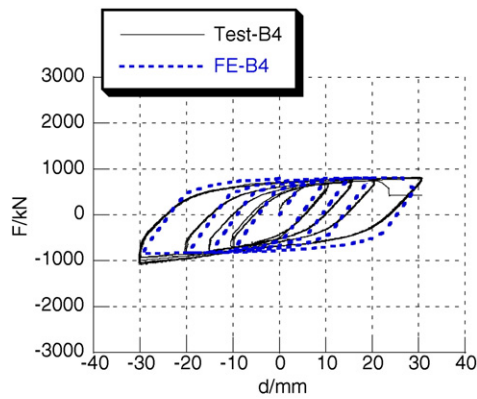
Fig. 9. Comparison between FE analysis and physical test.

Eq. (7) describes the constraint effect of the constraint units. A value of  $\zeta \geq 1$  can protect the BRB from global buckling.  $P_{cr}$  is the critical axial load and  $F_y$  is the yield force of the kernel unit.  $E_i I_i$  and  $E_0 I_0$  are the bending stiffness of the kernel unit and constraint units, respectively.  $\mu_i L_i$  and  $\mu_0 L_0$  are the effective lengths of the kernel unit and constraint units.  $A_i$  and  $f_y$  are the area and yield force of the kernel unit, respectively.

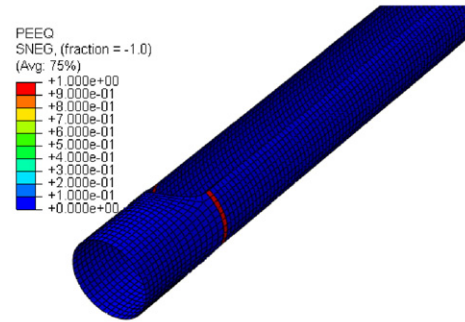
In this study, B2 and B5 had the same constraint units but different kernel units. Therefore, the Euler buckling modes and Euler

buckling load of the kernel unit are important to the constraint effect. As shown in Fig. 7, a model of the middle tube of B2 and B5 was established, designated as S4R in ABAQUS, where the out-of-plane deformation was not constrained. The top and bottom of the model were fixed. Euler buckling analysis was conducted to compare the constraint effects of B2 and B5.

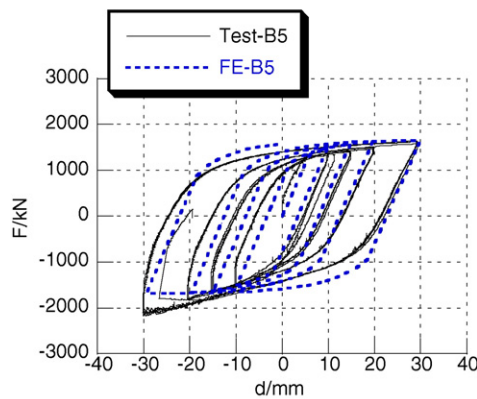
Fig. 11 compares the first four buckling modes of the middle units without constraints for B2 and B5. As shown in Fig. 11(a) and (b), respectively, significant buckling occurs at the fourth mode for B2, whereas



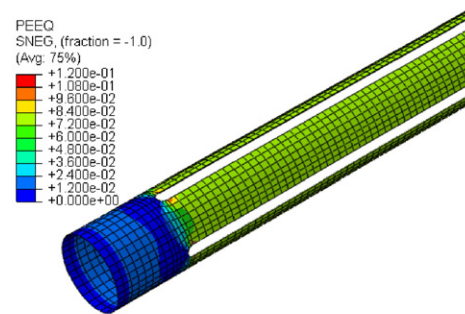
(g) Hysteresis curve of B4



(h) PEEQ distribution of B4



(i) Hysteresis curve of B5



(j) PEEQ distribution of B5

Fig. 9 (continued).

it occurs at the first mode for B5. These observations indicate that the middle unit of B2 has much better stability than that of B5. The critical axial load of the middle units of B2 and B5 are compared in Table 6. The critical axial load of the B2 is much larger than that of the B5. Therefore, the global buckling of B5 will occur much earlier than B2, which agree with the physical tests results, i.e. B2 with  $2 \times 2$  slotted holes performed better than B5 with  $2 \times 4$  slotted holes. Based on the test and analysis results, less number of slotted holes is preferred, and  $2 \times 2$  slotted holes are recommended to maintain the symmetry.

#### 4. Conclusion

A new BRB comprising three tubes with slotted holes arranged on the middle tube was proposed. Physical tests were conducted on five different specimens to investigate the effect of the size and number of the slotted holes on the performance of the new BRB. Additionally, FE analyses were carried out to explain the tests results. Major findings obtained from this study are as follows:

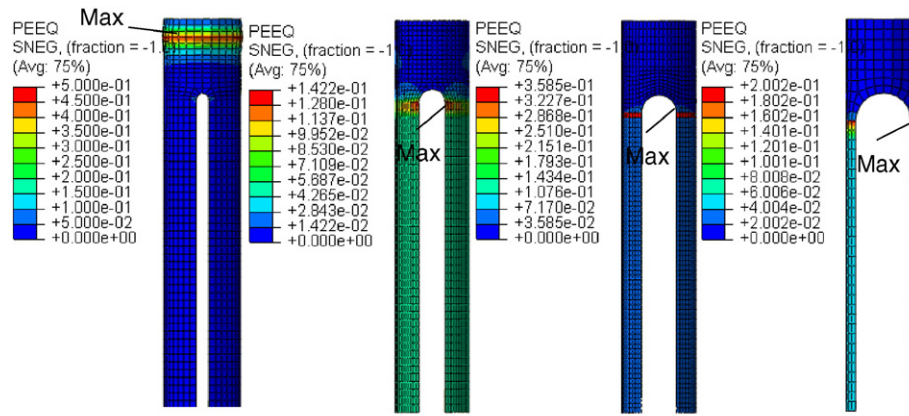
- (1) There are three main failure modes of the BRB: local buckling at the end with no constraint, tension failure at the slotted hole and global buckling. The slotted holes arranged on the middle tube are the main deformation field.
- (2) The BRB with appropriate design, e.g. B2, exhibits excellent performance in terms of its deformation capacity and low-cycle fatigue behavior. The hysteresis curves are stable and saturated,

corresponding to an equivalent ratio of critical viscous damping of 0.40 at the loading amplitude of  $1/100L$ .

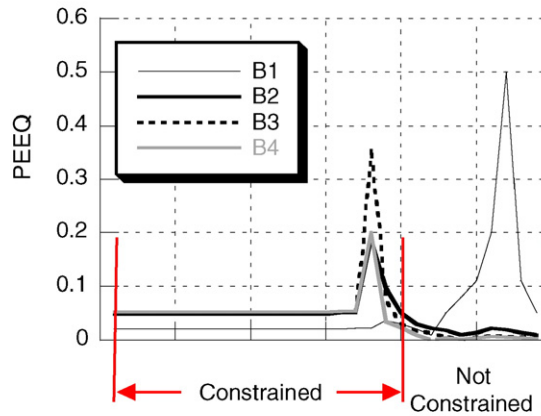
- (3) With the help of finite element analysis, the effect of the opening-hole ratio was concluded. When the opening-hole ratio is lower e.g. B1, the deformation at the unconstrained end is larger. Finally, local buckling occurs at the unconstrained end because of the strengthening of the slotted-hole field. When the opening-hole ratio is larger, e.g. B3 and B4, the deformation is concentrated to the slotted holes and deformation is concentrated at the end of it where fracture occurs. An opening-hole ratio of 0.2 is recommended for the design of the BRB.
- (4) According to the physical tests and finite element analysis, for the same opening-hole ratio, increasing the opening-hole number will lower the bending stiffness, which results in earlier global buckling, e.g. B5. Less number of slotted holes is recommended, and  $2 \times 2$  slotted holes arranged on the middle tube are recommended to maintain the symmetry.

#### Acknowledgements

The authors gratefully acknowledge the financial support from National key Basic Research Program of China (973 Program) under grant no. 012CB026204, and the Natural Science Foundation of China under grant nos. 51422809 and 51578314. Financial support from Tsinghua University Initiative Scientific Research Program under grant no. 2014z22067 is also appreciated.

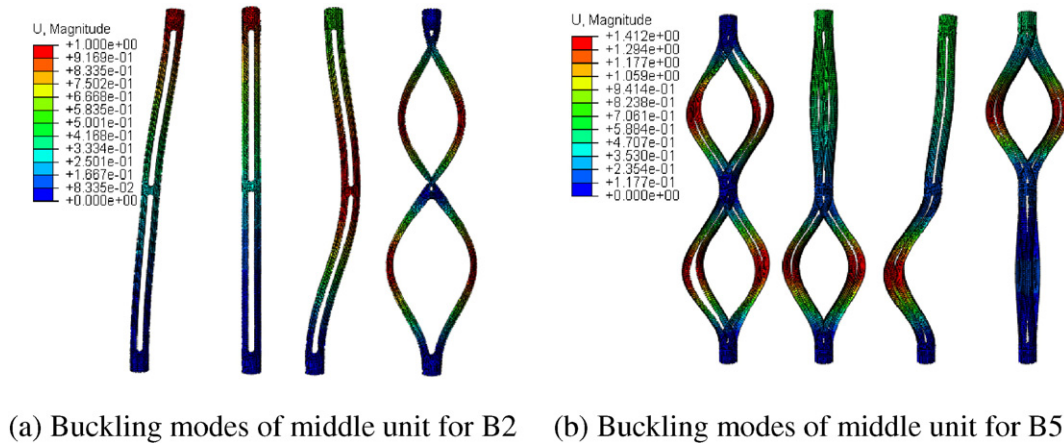


(a) PEEQ distribution of B1~B4



(b) PEEQ distribution curve of B1~B4

Fig. 10. Comparison of PEEQ between FE analysis for B1–B4.



(a) Buckling modes of middle unit for B2

(b) Buckling modes of middle unit for B5

Fig. 11. Comparison on buckling modes of middle units for B2 and B5.

Table 6  
Critical axial load of the middle units of B2 and B5.

No. mode	1	2	3	4
Middle unit-B2/kN	339.86	348.64	641.37	1671.8
Middle unit-B5/kN	270.64	281.46	281.57	282.64

References

- [1] E.M. Marino, M. Nakashima, Seismic performance and new design procedure for chevron-braced frames [J], Earthq. Eng. Struct. Dyn. 35 (4) (2006) 433–452.
- [2] M. Bosco, E.M. Marino, Design method and behavior factor for steel frames with buckling restrained braces [J], Earthq. Eng. Struct. Dyn. 42 (8) (2013) 1243–1263.
- [3] P. Pan, L.P. Ye, W. Shi, et al., Engineering practice of seismic isolation and energy dissipation structures in China [J], SCIENCE CHINA Technol. Sci. 55 (11) (2012) 3036–3046.

- [4] Y. Takeda, Y. Kimura, K. Yoshioka, et al., An experimental study on braces encased in steel tube and mortar [C], Annual Meeting Architectural Institute of Japan 1976, pp. 1041–1042.
- [5] S. Kuwahara, M. Tada, T. Yoneyama, et al., A study on stiffening capacity of double-tube members [J], *J. Struct. Constr. Eng.* 445 (3) (1993) 151–158.
- [6] T. Suzuki, T. Ogawa, T. Ogasawara, A study on inelastic buckling of circular tubes under axial compression with outer constraints [J], *J. Struct. Constr. Eng. AIJ* 458 (4) (1994) 137–143.
- [7] K. Takeita, K. Nagao, T. Taguchi, Studies on buckling-restrained bracing using triple steel tubes: part 2: consideration on experimental results and finite element method analysis [C], Summaries of Technical Papers of Annual Meeting Architectural Institute of Japan, C-1, Architectural Institute of Japan, Tokyo 2005, pp. 1013–1014.
- [8] H. Hasegawa, T. Takeuchi, M. Iwata, et al., Experimental study on dynamic behavior of unbonded braces [J], *J. Archit.* 114 (1448) (1999) 103–106.
- [9] Y. Koetaka, T. Kinoshita, K. Inoue, et al., Criteria of buckling-restrained braces to prevent out-of-plane buckling [C], The 14th World Conference on Earthquake Engineering, 2008 12-1.
- [10] Q. Xie, State of the art of buckling-restrained braces in Asia [J], *J. Constr. Steel Res.* 61 (6) (2005) 727–748.
- [11] N. Hoveidae, B. Rafezy, Global buckling behavior of all-steel buckling restrained braces [J], *J. Constr. Steel Res.* 79 (2012) 151–158.
- [12] C.H.E.N.G. Guangyu, Y.E. Lieping, X.U. Xiuzhen, C.U.I. Hongchao, Experimental research on buckling-restrained brace [J], *J. Build. Struct.* 29 (1) (2008) 31–39 (In Chinese).
- [13] W.A.N.G. Xiaolan, G.U.O. Yanlin, J.I.A.N.G. Ziqin, Behavior and design method of pinned-pinned buckling-restrained brace [J], *J. Build. Struct.* 34 (7) (2013) 97–106 (In Chinese).
- [14] G.U.O. Yanlin, W.A.N.G. Xiaolan, J.I.A.N.G. Ziqin, Behavior and design method of fixed-fixed buckling-restrained brace [J], *J. Build. Struct.* 34 (7) (2013) 107–118 (In Chinese).
- [15] Y.I.N. Zhan-zhong, W.A.N.G. Xiu-li, L.I. Xiao-dong, Finite element analysis of double-steel-tube buckling restricting braces with contact-ring [J], *J. Lanzhou Univ. Technol.* 5 (2008) 122–126 (In Chinese).
- [16] D.E.N.G. Xuesong, C.H.E.N. Zhen, Z.H.O.U. Yun, Experimental study on performance of perforating triple-steel tube buckling-restrained brace [J], *J. Build. Struct.* 33 (6) (2012) 42–49 (In Chinese).
- [17] X. Deng, Z. Zhengmin, Z. Yun, Experimental and finite-element studies of notched triple-steel tube buckling-resistant brace [J], *China Civ. Eng. J.* 43 (12) (2010) 41–49 (In Chinese).
- [18] S. Merritt, C.M. Uang, G. Benzoni, Subassembly testing of corebrace buckling-restrained braces [J], Final Report to CoreBrace, LLC, Department of Structural Engineering, University of California, San Diego, 2003.
- [19] GB 50011–2010, Code for Seismic Design of Buildings [S], China Architecture & building Press, Beijing, 2010 (In Chinese).
- [20] Y. Shi, M. Wang, Y. Wang, Experimental and constitutive model study of structural steel under cyclic loading [J], *J. Constr. Steel Res.* 67 (8) (2011) 1185–1197.
- [21] K. Deng, P. Pan, J. Sun, et al., Shape optimization design of steel shear panel dampers [J], *J. Constr. Steel Res.* 99 (2014) 187–193.
- [22] K. Deng, P. Pan, W. Li, et al., Development of a buckling restrained shear panel damper [J], *J. Constr. Steel Res.* 106 (2015) 311–321.
- [23] ABAQUS, Inc., ABAQUS Analysis Reference Manual 2010 3, ABAQUS Analysis User's Manual, ABAQUS, Inc., 2010.
- [24] J. Black, N. Makris, D. Aiken, Component testing, seismic evaluation and characterization of buckling-restrained braces [J], *J. Struct. Eng.* 130 (6) (2004) 880–894.